

A MULTIZONE MODEL FOR SIMULATING THE HIGH-ENERGY VARIABILITY OF TeV BLAZARS

PHILIP B. GRAFF,¹ MARKOS GEORGANOPOULOS,^{1,2} ERIC S. PERLMAN,³ AND DEMOSTHENES KAZANAS²

Received 2007 July 10; accepted 2008 August 12

ABSTRACT

We present a time-dependent multizone code for simulating the variability of synchrotron self-Compton (SSC) sources. The code adopts a multizone pipe geometry for the emission region, appropriate for simulating emission from a standing or propagating shock in a collimated jet. Variations in the injection of relativistic electrons in the inlet propagate along the length of the pipe, cooling radiatively. Our code for the first time takes into account the nonlocal, time-retarded nature of SSC losses that are thought to be dominant in TeV blazars. The observed synchrotron and SSC emission is followed self-consistently, taking into account light-travel time delays. At any given time, the emitting portion of the pipe depends on the frequency and the nature of the variation followed. Our simulation employs only one additional physical parameter relative to one-zone models, that of the pipe length, and is computationally very efficient, using simplified expressions for the SSC processes. The code will be useful for observers modeling *Fermi*, TeV, and X-ray observations of SSC blazars.

Subject headings: galaxies: active — quasars: general — radiation mechanisms: nonthermal — X-rays: galaxies

1. INTRODUCTION

In blazars, radio-loud active galaxies with their relativistic jets pointing close to our line of sight (Blandford 1978), the observed radiation is dominated by relativistically beamed emission from the subparsec base of the jet. The blazar spectral energy distribution (SED) consists of two components. The first one, peaking at submillimeter to X-ray energies is almost certainly due to synchrotron radiation, while the second one, peaking at MeV to TeV energies, is believed to be of an inverse Compton (IC) nature, with both components produced by the same population of relativistic electrons. The nature of the IC-scattered seed photons is still not clear, with both external optical-UV photons from the broad-line region (Sikora et al. 1994) and IR photons from the putative molecular torus (Błażejowski et al. 2000), as well as synchrotron photons (SSC; e.g., Maraschi et al. 1992), contributing. It is believed that in the case of powerful blazars peaking at MeV to GeV energies, external seed photons from the broad-line region dominate the IC scattering, while for weaker lineless blazars, peaking at \sim TeV energies, SSC is the dominant emission mechanism. Recent observational results (e.g., D’Arcangelo et al. 2007; Marscher et al. 2008), however, place the blazar emission site beyond the broad-line region, lending support to the possibility that even in powerful blazars the GeV emission process may be pure SSC. For a review of leptonic models, as well as hadronic models for blazar emission (e.g., Aharonian 2000), see Böttcher (2007).

Because of the small angular size of the blazar emission region, it is not possible to spatially resolve the emitting region. Because of this, information about the structure of the emitting source can be obtained only through multiwavelength variability studies. Particularly telling is the variability of the emission produced by the highest energy electrons, because these electrons lose energy very quickly and exist only close to the sites where they have been produced. The goal of multiwavelength variabil-

ity campaigns, involving in many cases observations from radio up to TeV energies, is to study the characteristics of blazar variability, such as correlations and/or time delays between different energies, spectral characteristics of the observed variability, and the amplitude of variability as a function of energy.

Most notable among blazars are the so-called TeV blazars for which the synchrotron emission peaks at X-ray energies and the SSC emission peaks at TeV energies, as they present the active galaxies producing the highest confirmed electron energies. Variations of TeV blazars in these two bands can be extremely rapid (TeV doubling times as short as a few minutes; Aharonian et al. 2007), suggesting highly relativistic subparsec scale flows (Doppler factors $\delta \sim 50$; e.g., Begelman et al. 2008) that decelerate substantially (Georganopoulos & Kazanas 2003; Ghisellini et al. 2005) to match the much slower speeds required by VLBI observations (Piner & Edwards 2004; Piner et al. 2008). The TeV and X-ray variations are usually well correlated (e.g., Fossati et al. 2008; Maraschi et al. 1999; Sambruna et al. 2000), as expected, because they present variations by the same electron population. Usually, the lower energy emission within each of these bands peaks with small time delays relative to the higher energy emission (e.g., Fossati et al. 2000), while the X-ray and TeV spectra become harder with increasing flux (e.g., Takahashi et al. 1996). In certain cases, however, the X-ray and TeV variability do not seem to be correlated in a simple way (e.g., Aharonian et al. 2005). An intriguing variability pattern is that of the so-called orphan flares, rare TeV flares that are not accompanied by X-ray flares (e.g., Krawczynski et al. 2004; Błażejowski et al. 2005). While the correlated X-ray–TeV flares can be understood through an increase of the high-energy emitting electrons, orphan TeV flares defy such a straightforward explanation.

Models of blazar emission to date have, for the most part, been in some form of homogeneous one-zone models (e.g., Mastichiadis & Kirk 1997; Krawczynski et al. 2002). Such models, although appropriate for modeling the steady state emission of a source, cannot simulate variability faster than the zone light crossing time. The basic limitation of one-zone models stems from the fact that the high-energy variability of both the synchrotron and SSC components is produced by high-energy electrons with cooling times shorter than the light crossing time. Even if

¹ Department of Physics, Joint Center for Astrophysics, University of Maryland, Baltimore County, 1000 Hilltop Circle, Baltimore, MD 21250.

² NASA Goddard Space Flight Center, Code 663, Greenbelt, MD 20771.

³ Department of Physics and Space Sciences, Florida Institute of Technology, 150 West University Boulevard, Melbourne, FL 32901.

we assume that a disturbance in the radiating plasma (e.g., a higher density) instantaneously propagates across the zone, the received radiation would be smeared out for timescales shorter than the light crossing time, due to light-travel time delays from different parts of the source (§ 2.1; also Chiaberge & Ghisellini 1999), and no variability faster than the light crossing time would be observed. One, therefore, cannot use one-zone models to infer the source structure from high-energy variability.

Inhomogeneous variability models of increasing degrees of sophistication have attempted to overcome the problems of one-zone models. The basic idea is to overcome the unphysical instantaneous injection throughout the source by adopting a specific geometry for the plasma flow that includes an inlet for injecting the radiating plasma. Variations in the injected plasma propagate and produce variations in the emissivity. Calculations of the received emission that take into account the light-travel times that radiation from different parts of the source takes to reach the observer produce light curves that, at least, do not violate causality. How physically realistic these light curves are depends on the approximations used and on the characteristics of the source to be modeled. For example, synchrotron and IC losses from photons external to the source are local processes in the sense that, at a given point in the flow, the energy loss rate only depends on the local magnetic field and external photon field energy density, and not on the photon production throughout the source. This is not the case with SSC losses, because synchrotron photons produced throughout the source at earlier times—to take into account the light-travel time from one point of the source to another—contribute to the photon energy density responsible for the SSC losses and to the emissivity at a given point and time in the source. To properly model sources like TeV blazars, in which SSC losses are important or even dominant, these considerations have to be taken into account.

There have been a few attempts during the last fifteen years to take these spatial considerations into account. Gómez et al. (1994) considered a conical jet with a constant bulk Lorentz factor flow, in which the electron plasma and the magnetic field undergo adiabatic evolution only, and they calculated the radio variability induced by a shock wave propagating along the jet. Georganopoulos & Marscher (1998a, 1998b) studied a parabolic jet that hydrodynamically accelerates and focuses to a conical geometry, and by following the synchrotron energy losses of the emitting electrons, they reproduced the radio to X-ray light curves of the X-ray–bright blazar PKS 2155–304. This resulted in a frequency-dependent source size, in agreement with the fact that the variability timescale of synchrotron radiation increases with decreasing frequency. It also reproduced the usually observed soft lags (variations at soft X-rays being preceded by variations at hard X-rays) and the counterclockwise X-ray flux–X-ray spectral index loops (e.g., Takahashi et al. 1996; Maraschi et al. 1999; Kataoka et al. 2000; Ravasio et al. 2004), both manifestations of radiative cooling dominating the energetics of the high-energy electrons.

Kirk et al. (1998) developed a semianalytical model in which low-energy electrons are injected in a zone where they undergo acceleration and eventually escape. The acceleration zone is assumed to move with a certain velocity, leaving behind the freshly accelerated electrons that cool through synchrotron radiation. Variations in the injection rate of low-energy electrons in the acceleration zone result in variations of the emissivity, which are integrated over the volume of the source, taking into account time delays, to produce the observed multifrequency synchrotron light curves. This model includes a treatment of particle acceleration, and it is able to reproduce the uncommon hard lags

(variations at hard X-rays preceded by variations at soft X-rays) and clockwise X-ray flux–X-ray spectral index loops (Zhang 2002; Ravasio et al. 2004), both manifestations of electrons still accelerating, just before reaching the maximum electron Lorentz factor, where the acceleration and radiative loss timescales are comparable. It does not include, however, SSC considerations.

Chiaberge & Ghisellini (1999) studied the synchrotron and SSC emission from a homogeneous one-zone model in which they assumed an instantaneous plasma injection, but taking into account the time delays with which the external observer would observe the variability (a similar approach was also taken by Kataoka et al. 2000). They also studied a case similar to that of Kirk et al. (1998), but without treating particle acceleration, by splitting the source into smaller one-zone models that evolved autonomously, in the sense that (1) the SSC emission inside any one of their single zones uses as seed photons only the synchrotron photons produced in that zone and (2) the SSC energy losses in every zone are caused only by the synchrotron photons produced in that zone. This simplified approach is a good approximation for following the energetics of the electrons if the source is synchrotron dominated (because the SSC losses, although inappropriately calculated, are negligible), but does not produce realistic SSC light curves, because it does not calculate the emission due to upscattering synchrotron photons produced in other parts of the source in retarded times.

A significant improvement was introduced by Sokolov et al. (2004), who incorporated in the calculation of the SSC emission from a given location in an inhomogeneous source the synchrotron photons produced throughout the source in retarded times. This produces accurate SSC light curves, provided that the SSC losses that were still treated as a local process are negligible. In a followup paper, Sokolov & Marscher (2005) considered also external Compton photons from the broad-line region and the molecular torus. The challenge for inhomogeneous multizone models for sources such as the TeV-emitting blazars is the calculation of the nonlocal, time-retarded SSC losses induced by photons produced in other parts of the source.

Here, we present such an inhomogeneous model that, for the first time, takes into account the effect of the nonlocal, time-delayed source emission on the SSC losses. We assume that a power law of relativistic electrons is injected at the inlet of a pipe and that the electrons flow downstream and cool radiatively. Variations in the injected electron distribution propagate downstream and manifest themselves as frequency-dependent variability. This allows us to model high-energy multiwavelength variability in a self-consistent manner. In § 2 we describe the one-zone model, which we use as a building block for the multizone model, and we show that, by construction, one-zone models cannot simulate the variability produced by high-energy electrons with radiative cooling times shorter than the electron light crossing time from the single zone. In § 3 we describe our multizone, pipe geometry model with emphasis on the coupling between subsequent zones and on the calculation of the local photon field due to nonlocal, time-delayed emission throughout the source. This is followed in § 4 by a comparison of the code with analytical results and a series of case studies. We conclude in § 5 with a discussion of additional considerations that can be used as starting points for future work.

2. THE ONE-ZONE MODEL

We consider a homogeneous spherical source of radius R permeated by a magnetic field B of energy density $B^2/(8\pi)$. Energetic electrons are injected into the region at a rate $q(\gamma, t)$, where γ is the electron Lorentz factor and t is the injection

time. These electrons lose energy through synchrotron and IC radiation and eventually escape after a characteristic time, t_{esc} , of the order of the light crossing time. The implementation we describe is applicable to sources that are optically thin both to synchrotron emission in the frequency range under consideration and to γ -ray absorption due to pair production.

The kinetic equation that describes the time evolution of the electron energy distribution (EED) $n(\gamma, t)$ is

$$\frac{\partial n(\gamma, t)}{\partial t} + \frac{\partial}{\partial \gamma} [\dot{\gamma} n(\gamma, t)] + \frac{n(\gamma, t)}{t_{\text{esc}}} = q(\gamma, t). \quad (1)$$

Here, $\dot{\gamma}$ includes both the synchrotron losses $\dot{\gamma}_s$ and the IC losses $\dot{\gamma}_{\text{IC}}$ in the Thomson regime ($\epsilon \leq 3/4$),

$$\begin{aligned} \dot{\gamma} &= \dot{\gamma}_s + \dot{\gamma}_{\text{IC}}, & \dot{\gamma}_s &= \frac{4\sigma_{\text{T}}}{3mc} \gamma^2 U_B, \\ \dot{\gamma}_{\text{IC}} &= \frac{4\sigma_{\text{T}}}{3mc} \gamma^2 \int_{\epsilon_{\text{min}}}^{\min[\epsilon_{\text{max}}, 3/(4\gamma)]} U(\epsilon, t) d\epsilon, \end{aligned} \quad (2)$$

where $U(\epsilon, t)$ is the photon field energy density, ϵ is the photon energy in units of the electron rest energy $m_e c^2$, and σ_{T} is the Thomson cross section. The photon field $U(\epsilon, t)$ includes not only the synchrotron-produced photons, but all the photons produced in the source through IC scattering, including, therefore, all the higher order SSC emission.

We calculate the synchrotron emission following Melrose (1980),

$$\begin{aligned} L_s(\epsilon_s, t) &= 1.85 \frac{\sqrt{2} q^3 B}{h} \int_{\gamma_{\text{min}}}^{\gamma_{\text{max}}} z^{1/3} e^{-z} n(\gamma, t) d\gamma, \\ z &= (2/3)^{1/2} \epsilon_s / B_* \gamma^2, \end{aligned} \quad (3)$$

where q is the electron charge, $B_* = B/B_{\text{crit}}$, and $B_{\text{crit}} = (m_e^2 c^3)/(eh)$ is the critical magnetic field where the electron cyclotron energy equals its rest mass and strong field considerations become important (e.g., Harding & Lai 2006). We note that, although a δ -function approach for calculating the synchrotron emissivity would be faster, it would misinterpret the spectra in cases of hard power-law injection $q \propto \gamma^{-p}$ ($p > 2$), whose cooling is known to produce a pileup at its high-energy cutoff (e.g., Kardashev 1962). Also, a δ -function synchrotron emissivity would not produce the $f_\nu \propto \nu^{1/3}$ spectrum at frequencies below the critical frequency of the lowest energy electrons. These lower energy photons can be important seed photons for producing hard SSC TeV emission as Katarzyński et al. (2006) point out.

To obtain the SSC emission through a simple integration as in the synchrotron case, we employ the δ -function approximation in which seed photons of energy ϵ_0 are IC scattered by electrons of Lorentz factor γ to energy $\epsilon_{\text{IC}} = (4/3)\epsilon_0\gamma^2$, as long as the scattering takes place in the Thomson regime ($\gamma\epsilon_0 < 3/4$). If we consider seed photons in the energy range $d\epsilon_0$ being IC scattered by electrons with Lorentz factors in the range $d\gamma$, then the emitted IC power is $\dot{\gamma}_{\text{IC}} m_e c^2 n(\gamma, t) d\gamma$ and it is spread over a final photon energy range $d\epsilon_{\text{IC}} = 4(\epsilon_0\epsilon_{\text{IC}}/3)^{1/2} d\gamma$, resulting in an IC specific luminosity per seed photon energy interval,

$$\begin{aligned} dL_{\text{IC}}(\epsilon_{\text{IC}}, t) &= m_e c^2 n(\gamma, t) \dot{\gamma}_{\text{IC}} (d\gamma/d\epsilon_{\text{IC}}) \\ &\times \delta(\gamma - (3\epsilon_{\text{IC}}/4\epsilon_0)^{1/2}) \Theta(3/4 - \gamma\epsilon_0), \end{aligned} \quad (4)$$

where in this context $\dot{\gamma}_{\text{IC}} = (4\sigma_{\text{T}}/3mc)\gamma^2 U(\epsilon_0, t) d\epsilon_0$ and $\Theta(x)$ is the Heaviside step function. This is written as

$$\begin{aligned} dL_{\text{IC}}(\epsilon_{\text{IC}}, t) &= 3^{1/2} \sigma_{\text{T}} c n(\gamma, t) U(\epsilon_0, t) d\epsilon_0 \epsilon_{\text{IC}}^{1/2} / (4\epsilon_0^{3/2}) \\ &\times \delta(\gamma - (3\epsilon_{\text{IC}}/4\epsilon_0)^{1/2}) \Theta(3/4 - \gamma\epsilon_0). \end{aligned} \quad (5)$$

Integrating over the available seed photon distribution, we obtain

$$\begin{aligned} L_{\text{IC}}(\epsilon_{\text{IC}}, t) &= (3^{1/2} \sigma_{\text{T}} c \epsilon_{\text{IC}}^{1/2} / 4) \\ &\times \int_{\epsilon_{0,\text{min}}}^{\epsilon_{0,\text{max}}} n(\gamma, t) U(\epsilon_0, t) \epsilon_0^{-3/2} \delta(\gamma - (3\epsilon_{\text{IC}}/4\epsilon_0)^{1/2}) d\epsilon_0. \end{aligned} \quad (6)$$

The range of final photon energies ϵ_{IC} is $(4/3)\epsilon_{\text{seed},\text{min}}\gamma_{\text{min}}^2 < \epsilon_{\text{IC}} < \gamma_{\text{max}}$. For ϵ_{IC} within this range the limits of the above integration are

$$\epsilon_{0,\text{min}} = \begin{cases} \epsilon_{\text{seed},\text{min}}, & \epsilon_{\text{IC}} \leq \frac{4}{3} \epsilon_{\text{seed},\text{min}} \gamma_{\text{max}}^2, \\ \frac{3\epsilon_{\text{IC}}}{4\gamma_{\text{max}}^2}, & \epsilon_{\text{IC}} \geq \frac{4}{3} \epsilon_{\text{seed},\text{min}} \gamma_{\text{max}}^2, \end{cases} \quad (7)$$

$$\epsilon_{0,\text{max}} = \begin{cases} \frac{3\epsilon_{\text{IC}}}{4\gamma_{\text{min}}^2}, & \epsilon_{\text{IC}} \leq \gamma_{\text{min}} \\ \frac{3}{4\epsilon_{\text{IC}}}, & \epsilon_{\text{IC}} \geq \gamma_{\text{min}}. \end{cases} \quad (8)$$

Following Chang & Cooper (1970) and Chiaberge & Ghisellini (1999), we discretize the kinetic equation (1), using a grid of logarithmically spaced Lorentz factors, $\gamma_j, j = 0, 1, 2, \dots, j_{\text{max}}$, and linearly spaced time indices, t_i . The difference equation that describes this system is

$$\begin{aligned} \frac{n_{j,i+1} - n_{j,i}}{\Delta t} &= - \frac{\dot{\gamma}_{j+1,i+1} n_{j+1,i+1} - \dot{\gamma}_{j,i+1} n_{j,i+1}}{\Delta \gamma} \\ &+ q_{j,i+1} - \frac{n_{j,i+1}}{t_{\text{esc}}}. \end{aligned} \quad (9)$$

Note that this is an implicit scheme, in the sense that the calculation of $n_{j,i+1}$ requires knowledge of not only the previous time step EED, but also $n_{j+1,i+1}$, the next higher γ grid point at the current time. It is due to the implicit nature of the numerical procedure that this scheme is stable for large time steps. The difference equation can be written as a system of tridiagonal equations,

$$n_{j,i+1} = a n_{j,i} - b n_{j+1,i+1} + c q_{j,i+1}, \quad (10)$$

$$\begin{aligned} a &= \frac{\Delta \gamma}{\Delta \gamma + \Delta t \Delta \gamma / t_{\text{esc}} - \Delta t \dot{\gamma}_{j,i+1}}, \\ b &= a \frac{\Delta t}{\Delta \gamma} \dot{\gamma}_{j+1,i+1}, \quad c = a \Delta t. \end{aligned} \quad (11)$$

This can be easily computed if we use the initial condition $n_{j,0} = 0 \forall j$ (start with no relativistic electrons in the system) and the boundary condition $n_{j_{\text{max}},t} = 0 \forall t$. The first condition implies that the initial photon field is also zero for all photon energies. The second condition is satisfied if we set $\gamma_{j_{\text{max}}} > \gamma_{\text{max}}$, because the electrons can only lose energy, and there is no way to move to higher energies, populating the j_{max} bin of the γ -grid. The simulation proceeds in the following manner. Given $n(\gamma, t_i)$ and

$U(\epsilon_0, t_i)$ we first calculate $n(\gamma, t_{i+1})$. We then calculate the synchrotron luminosity, $L_S(\epsilon, t_{i+1})$, and the IC luminosity, $L_{IC}(\epsilon, t_{i+1})$. The specific photon energy density $U(\epsilon_0, t_{i+1})$ for the next time step is obtained by adding these two luminosities and dividing by $4\pi R^2 m_e c^3$.

2.1. Problems of One-Zone Models in Reproducing High-Energy Variability

By construction, in the one-zone model variations in the injection propagate instantaneously throughout the source, because no spatial coordinate enters the description of the system. If a power-law EED, $q \propto \gamma^{-p}$, $\gamma_{\min} \leq \gamma \leq \gamma_{\max}$, is injected in the source, radiative cooling and electron escape will result in a broken power-law EED $n(\gamma)$ in the source, steepening from an electron index p to $p + 1$, above γ_b , the electron Lorentz factor for which the escape time equals the radiative loss time,

$$\frac{\gamma_b}{\dot{\gamma}} = t_{\text{esc}} \Rightarrow \gamma_b = \frac{3m_e c}{4\sigma_T U t_{\text{esc}}}, \quad (12)$$

where U stands for the total photon and magnetic field energy density in the source. It is these electrons, with $\gamma > \gamma_b$, that produce the high-energy synchrotron and IC emission. Because the electron escape time is of the order of the light crossing time, $t_{\text{esc}} = kt_{lc} = kR/c$, $k \sim 1$ to a few, electrons with Lorentz factors $\gamma > \gamma_{lc} = k\gamma_b$ have a cooling time shorter than the light crossing time. One therefore anticipates that even for an injection event lasting much less than t_{lc} , the high-energy variable emission produced by electrons with $\gamma > \gamma_{lc}$ will be smeared out by light-travel time effects and would appear to last for $\sim t_{lc}$, even though at each point in the source it lasts a shorter time $\sim t_{lc}\gamma_{lc}/\gamma$.

To demonstrate this, a flaring state was simulated by an increase by a factor of 5 in the injection $q(\gamma, t)$ that lasted $t_{\text{inj}} = t_{lc}/10$. The system was allowed to reach a steady state before the disturbance in the injection was introduced. The emitted luminosity as a function of frequency was followed in time, allowing us to produce light curves. By not taking into account time delays and wrongly assuming that at any given time the observer sees the entire source as being at a single physical state, electrons with $t_{\text{cool}} < t_{lc}$ produce high-energy synchrotron and SSC variations that last less than t_{lc} (Fig. 1, *top*).

To take time delays into account, one has to consider that if at a certain time t the observer receives photons from the nearest (front) part of the source, slices further away from the observer will be seen as they were at retarded times $t - r/c$, where r is the distance of the slice from the front part of the source. To treat this, at each time the luminosity of the system was recorded for a number of time steps covering a time equal to the light crossing time of the region. The luminosity observed at any time is thus the sum of the luminosity from each of these time steps, as each one represents the light emitted by a slice sequentially further back from the observer. The resulting light curves, plotted in the bottom panel of Figure 1, show that when the size of the region and, thus, the time taken by light to travel across it are accounted for, the observed variability of high-energy electrons with $t_{\text{cool}} < t_{lc}$ is spread out over the length of the light crossing time. This is similar to what Chiaberge & Ghisellini (1999) observed when they performed a similar test.

Another serious problem stemming from the lack of spatial considerations in the one-zone model comes from the fact that the model by construction assumes that the photons produced in the source at a given time are instantaneously available as seed photons for IC scattering throughout the source. This unphysical assumption has serious implications on the calculation of the

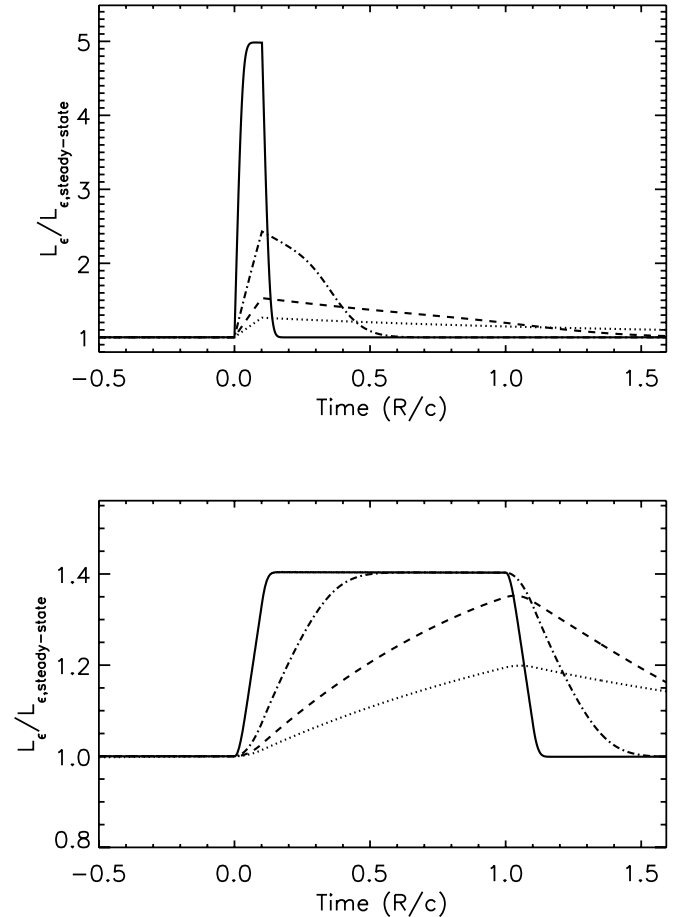


FIG. 1.— Short variation by a factor of 5 for $t_{\text{inj}} = t_{lc}/10$ and $t_{lc} = R/c$ introduced in the one-zone model. The dotted line tracks the synchrotron emission of the low-energy electrons with cooling time $t_{\text{cool}} > t_{\text{esc}}$, the dashed line of electrons with $t_{lc} < t_{\text{cool}} < t_{\text{esc}}$, the dash-dotted line of electrons with $t_{\text{inj}} < t_{\text{cool}} < t_{lc}$, and the solid line of electrons with $t_{\text{cool}} < t_{\text{inj}}$. *Top*: No light crossing delays are taken into account and this results in the unphysical result of variability times shorter than t_{lc} , for radiation produced by electrons with $t_{\text{cool}} < t_{lc}$. *Bottom*: Same event with light crossing delays taken into account. In this case, the light crossing time is the smallest observable variability scale. The time-integrated emission in the disturbance is the same in both cases, as can be easily seen for the highest frequency that reaches a plateau in both panels, $(5 - 1) \times 0.1 = (1.4 - 1) \times 1$.

SSC emissivity and on the calculation of the SSC losses, which in turn affect the evolution of the EED in the source and, through this, the entire spectrum and light curves. The first effect has been addressed by the inhomogeneous model of Sokolov et al. (2004) and Sokolov & Marscher (2005). We present now the first multi-zone simulation that incorporates the issue of light-travel time effects on the SSC losses.

3. THE MULTIZONE MODEL

3.1. The Flow Geometry

The simplest and least computationally intensive deviation from a homogeneous model that can address the issues discussed above is one in which plasma is injected into a pipe of radius R and length L and cools radiatively as it flows downstream before it escapes after traversing the pipe length. Physically, this resembles the situation of a standing or propagating shock, as seen in the frame of the shock front. The plasma flow velocity u and the magnetic field B are constant along the pipe, and the EED is assumed to have no lateral gradients along the cross section of the pipe. Relativistic plasma is injected at the base of the flow. The injection variation timescale in this geometry can be arbitrarily

smaller than R/c without violating causality, because, in principle, a disturbance in the plasma flow can reach the entire cross section of the inlet at a single time. However, the discretization procedure we describe below limits the range of meaningful injection variability to timescales greater than the plasma flow time through a zone of the flow. Our goal is to calculate the EED in the frame of the pipe as a function of time and distance z from the inlet of the pipe and, through this, calculate the emission received by an observer located at an angle θ to the axis of the pipe.

3.2. The Discretization of the Pipe

The pipe is broken down lengthwise, and all cells are of length l , comparable to the pipe radius R . The length of the pipe $L = Nl$, where N is the number of cells. Each cell is then simulated by a one-zone model. The electron injection at the first cell is $q_1(\gamma, t)$, similar to that defined for the one-zone model. In each time step, the electrons that are calculated to leave each cell are injected into the next cell in line in the next time step. The injection of electrons, therefore, in cell i at time t_j is $q_i(\gamma, t_j) = n_{i-1}(\gamma, t_{j-1})/t_{\text{esc}}$, and the kinetic equation for the i th cell is

$$\frac{\partial n_i(\gamma, t_j)}{\partial t} + \frac{\partial}{\partial \gamma} [\dot{\gamma} n_i(\gamma, t_j)] + \frac{n_i(\gamma, t_j)}{t_{\text{esc}}} = \frac{n_{i-1}(\gamma, t_{j-1})}{t_{\text{esc}}}. \quad (13)$$

Because in a time $\sim t_{\text{esc}}$, the electron content of a cell is transferred to the next cell; t_{esc} is connected to the bulk flow velocity u through $t_{\text{esc}} = l/u$. We also use t_{esc} as the time step of our simulation. This ensures that the actual distance a disturbance in the electron distribution travels in a time step is equal to the bulk velocity times the time step size, by transferring in a time step the electron content of cell i to cell $i + 1$. The shortest variability timescale that can be simulated by this configuration is the single-cell escape time. This limits the highest energy electrons that can be followed accurately to those of Lorentz factor $\gamma_b = 3m_e c u / 4\sigma_T U l$, where U is the photon plus magnetic field energy density in the first cell (see eq. [12]), and through this, the highest energies of synchrotron and IC variations can be reproduced. The advantage of the pipe configuration relative to a homogeneous model of the same size is that the highest energy electron variability we can follow is not connected to the length of the entire pipe, but to the length of a single zone, a quantity that is N times shorter. This results in the pipe being able to track variations faster by N , following electrons more energetic by N , and synchrotron and SSC frequencies higher by N^2 , relative to a homogeneous model of size L . An early version of this approach was presented by Graff et al. (2007).

3.3. The Photon Energy Density

To solve the kinetic equation for each cell, an expression for the photon energy density resulting from all other cells by taking into account light-travel time delays is required. In general, for a region S characterized by a time-dependent emission coefficient $j(\mathbf{r}', t', \epsilon)$, the photon energy density $U(\mathbf{r}, t, \epsilon)$ is calculated by integrating $j(\mathbf{r}', t', \epsilon)/c$ in retarded times over the volume of the region S . Setting $\mathbf{r} = 0$, for a point of interest in S , yields, without loss of generality,

$$U(\mathbf{r} = 0, t, \epsilon) = \frac{1}{c} \int_0^{r'(\Omega)} j(\mathbf{r}', t' = t - r'/c, \epsilon) dr' d\Omega. \quad (14)$$

For our geometry we express this through the following approximation. Consider a cell i centered at z_i being illuminated by a cell m

centered at z_m . The solid angle subtended at z_i by the cell m is $\Delta\Omega \approx \pi R^2 / (z_i - z_m)^2$. The photon energy density $\Delta U(z_i, z_m, t, \epsilon)$ at (z_i, t) due to photons produced at z_j at retarded time $t' = t - |z_i - z_m|/c$ is

$$\Delta U(z_i, z_m, t, \epsilon) = \frac{j(z_m, t' = t - |z_i - z_m|/c, \epsilon)}{c} \frac{\pi R^2}{(z_i - z_m)^2} l. \quad (15)$$

Making use of the fact that the volume of each cell is $V_c = \pi R^2 l$ and that the luminosity $L(\epsilon)$ emitted from a cell is $L(\epsilon) = 4\pi j(\epsilon) V_c$, we obtain

$$\Delta U(z_i, z_m, t, \epsilon) = \frac{L(z_m, t' = t - |z_i - z_m|/c, \epsilon)}{4\pi c (z_i - z_m)^2}. \quad (16)$$

A summation over all cells in the pipe results in the total photon energy density $U(z_i, t_j, \epsilon_k)$ at cell i , time $t_j = j t_{\text{esc}}$, and energy ϵ_k ,

$$U(z_i, t_j, \epsilon_k) = \frac{L(z_i, t_j, \epsilon_k)}{2\pi c R(R + l)} + \sum_{m=0, m \neq i}^N \frac{L(z_m, t' = j t_{\text{esc}} - |i - m|l/c, \epsilon_k)}{4\pi c l^2 (i - m)^2}, \quad (17)$$

where the first term is the photon energy density due to cell i itself. Note that a calculation of the photon energy density requires keeping record of a data cube of the SED emitted by each cell at each time for a number of time steps equal to the light crossing time of the entire region.

3.4. Pipe Orientation

When calculating the observed luminosities, we must take into account the different distances that light must travel from each of the different cells in the pipe to the observer. This difference is a function of the angle θ formed between the pipe and the observer. If photons emitted from the first cell are received by the observer at a given time, photons from cell i that are received simultaneously were emitted earlier by $il \cos \theta / c$. Beaming can be easily included in this model by assuming that the entire pipe is moving with a relativistic velocity along its axis. Then for a choice of bulk Lorentz factor Γ and orientation angle θ_{obs} in the observer's frame, one can calculate the Doppler factor δ and the angle θ in the frame of the pipe and transform the arrival times by dividing by δ , the observed frequencies by multiplying by δ , and the observed fluxes by multiplying by δ^3 .

4. RESULTS

4.1. Comparison with Analytical Results for the Synchrotron-dominated Case

A simple analytical test can be performed in the case of a source in which the energy losses are dominated by synchrotron radiation. In this case, adopting a steady power-law electron injection at the inlet and assuming an electron residence time kL/c in the source, the source-integrated EED will reach after time $t \gg kL/c$ a steady state. This steady state, source-integrated electron distribution is a broken power law with an electron index steepening by 1 at $\gamma_b = (3m_e c^2) / (4\sigma_T U_B kL)$. This will produce a synchrotron spectrum with a spectral break of 1/2 at an energy $\epsilon_b = B_* \gamma_b^2$. For the synchrotron-dominated configuration presented in Figure 2, the numerical result is in good agreement with the analytical result for both the EED and the SED employing a

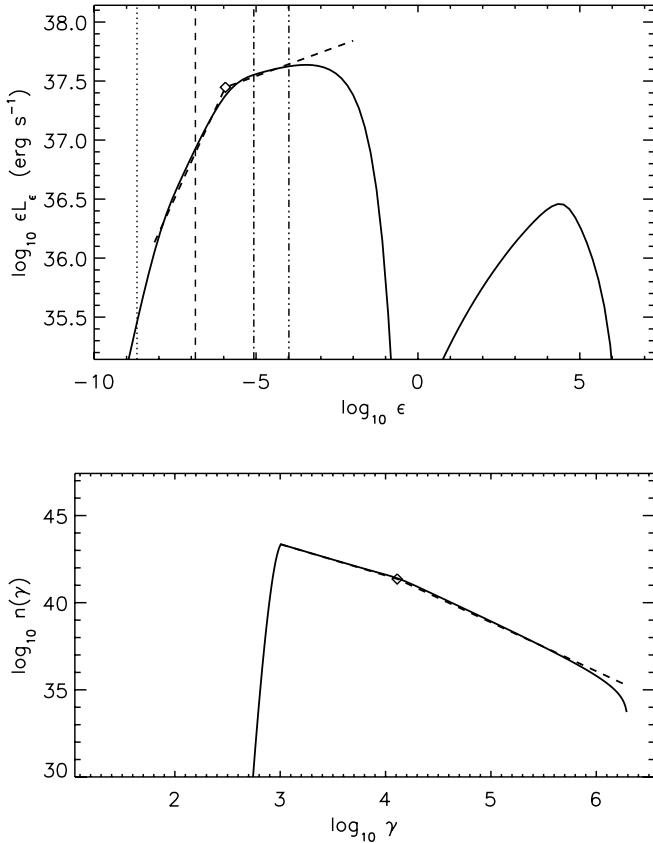


FIG. 2.— Comparison of the steady state numerical result with the analytical solution of a synchrotron-dominated configuration. The following parameters have been used: a pipe of length $L = 10^{16}$ cm and radius $R = 5 \times 10^{14}$ cm (aspect ratio 10 : 1). The magnetic field in the pipe is $B = 0.3$ G, and a power-law EED is continuously injected with $\gamma_{\min} = 10^3$, $\gamma_{\max} = 2 \times 10^6$, and $p = 1.8$. The pipe is split into 40 cylindrical slices of equal height $l = L/40 = 2.5 \times 10^{14}$ cm, and the escape time is set to $k = 2$ times the light crossing time. With these parameters fixed, the ratio of the SSC to synchrotron luminosity increases with increasing electron injected power, and for $L_{\text{inj}} = 5 \times 10^{38}$ ergs s^{-1} , the system is synchrotron dominated. *Bottom:* Plots of the analytical (*dashed line*) and numerical (*solid line*) steady state EED. *Top:* Plots of the analytical synchrotron (*dashed line*) and numerical (*solid line*) synchrotron and SSC SED. The four vertical lines mark four frequencies whose variability we study in Fig. 3 using the same line styles.

δ -function synchrotron emissivity. Note that the SSC luminosity is much lower than the synchrotron one. Note also that while the analytical synchrotron emission stops at $\epsilon_{\min} = B_* \gamma_{\min}^2$, the numerical continues to lower frequencies, due to the $f_\nu \propto \nu^{1/3}$ lower energy tail of the synchrotron emissivity.

To compare the variability of our code with analytic expectations, we initiate the injection of a power-law EED at $t = 0$ at the inlet and follow the evolution of the system toward a steady state. We expect that the EED will reach a steady state at or before a time $\sim kL/c = 2L/c$, equal to the time it takes for an electron to traverse the length of the pipe and escape, or equivalently, the time it takes to fill the pipe with electrons. The part of the EED with $\gamma < \gamma_b$ will reach a steady state at $\sim kL/c$, because the electrons responsible for this emission traverse the entire pipe without cooling appreciably.

At higher energies, $\gamma > \gamma_b$, the electron radiative cooling lifetime $t = (3m_e c)/(4\sigma_T U_B \gamma)$ is shorter than $t = kL/c$. Electrons, therefore, of progressively higher energy will be confined closer to the inlet, resulting in an energy-dependent pipe size. This, together with the orientation of the observer, determines the time it takes for the emission at a given energy to reach the steady state.

For an observation angle $\theta = \pi/2$, there will be no position-dependent delays, given that the light path from all parts of the pipe to the observer are equal. Note that if the source is moving relativistically with bulk Lorentz factor Γ , $\theta = \pi/2$ transforms to $\theta = 1/\Gamma$ in the observer's frame. At $\epsilon_s < \epsilon_b$ we expect a practically achromatic increase of the luminosity, reaching a steady state at $\sim kL/c$, because the electrons responsible for this emission have $\gamma < \gamma_b$. At higher energies $\epsilon_s > \epsilon_b$ the emission comes from electrons with energy $\gamma > \gamma_b$, and the time to reach steady state is $t = (3m_e c)/(4\sigma_T U_B \gamma) = (3m_e c B_*^{1/2})/(4\sigma_T U_B \epsilon_s^{1/2})$, where we have used $\epsilon_s = B_* \gamma^2$.

To verify that the model variability agrees with our analytical predictions, we select four synchrotron energies, marked by the four vertical lines in Figure 2. The lowest energy (dotted vertical line) comes entirely from the $\nu^{1/3}$ tail of the synchrotron emissivity, and it is heavily dominated by the lowest energy electrons with $\gamma = \gamma_{\min} \ll \gamma_b$ that have no time to cool before they escape. The second lower energy (dashed vertical line in Fig. 2) at $\epsilon_{\min} < \epsilon < \epsilon_b$ is predominately due to electrons with $\gamma_{\min} < \gamma < \gamma_b$ that also escape before they cool appreciably. In the top panel of Figure 3 we plot the model light curves of these two low synchrotron energies, using the same line styles. As expected, the two light curves are almost indistinguishable, both reaching a steady state at $t \sim 2L/c$ (marked by a solid vertical line in the top panel of Fig. 3).

The light curves of two more energies, this time with $\epsilon_s > \epsilon_b$, are marked by the dot-dashed and dot-dot-dashed lines in Figure 2 and are plotted in the top panel of Figure 3 using the same line styles. The vertical lines with the same line styles in Figure 3 indicate the time at which the corresponding light curves are expected to reach a steady state. As can be seen, at these times the light curves are at $\sim 80\%$ of their steady state level. This is mainly because electrons continue to radiate at a given energy ϵ_s even when their Lorentz factor drops below $(\epsilon_s/B_*)^{1/2}$, as the exponential decay of the emissivity indicates (eq. [3]; e.g., the synchrotron emissivity of an electron with Lorentz factor $\gamma = (\epsilon_s/B_*)^{1/2}$ at time t_0 drops $\propto \exp[-(t/t_0)^2]$ from its peak emissivity, requiring $t = 2t_0$ to drop by 98%). To verify this, we plot in the middle panel of Figure 3 the same light curves, using the δ -function approximation for the synchrotron emissivity. As can be seen, the two high-energy light curves approach the steady state level significantly closer to the analytically expected time.

To evaluate if the light-travel effects are properly taken into account, we rotate the pipe in such a way that the inlet is closer to the observer ($\theta = 0$), as is the case for a propagating shock that is observed “jet on.” In this case, we anticipate that the low-energy ($\epsilon < \epsilon_b$) variability that requires one to fill the entire pipe with plasma will reach a steady state after an additional time L/c , because this is the additional length that variations from the end of the pipe have to travel to reach the observer. The time it takes, therefore, for the lower energy emission steady state to be reached is $(k + 1)L/c$. For higher energy variability ($\epsilon > \epsilon_b$) that reaches a steady state before time $t < kL/c$, the additional light-travel time required is $(tc/k)/c = t/k$, where tc/k is the maximum distance from the inlet of the pipe that contributes to the energy under consideration. The time it takes, therefore, for the steady state to be reached is $t(1 + 1/k)$. We demonstrate these considerations in the bottom panel of Figure 3. As can be seen, the time it takes for the low energies ($\epsilon < \epsilon_b$) to reach steady state is now $(k + 1)L/c = 3L/c$, and the time it takes for the high-energy light curves to reach a steady state increases by a factor $\sim 1/2$, as can be seen by comparing the top and bottom panels of Figure 3 (e.g., the dot-dashed light curve reaches 95% of the steady state after $t \approx 1.1L/c$ for $\theta = \pi/2$ and after $t \approx 1.65L/c$ for $\theta = 0$).

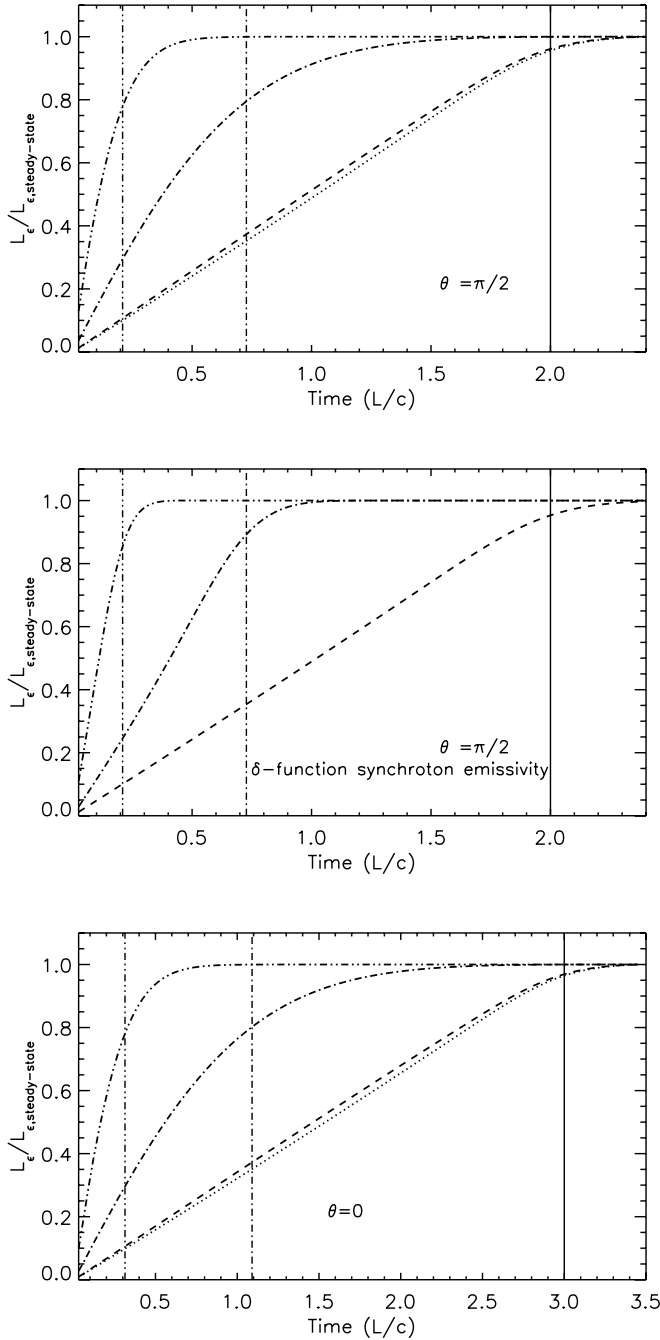


FIG. 3.—Light curves of the four frequencies shown by the vertical lines in Fig. 2, using the same line styles, for two different pipe orientations. The solid vertical lines correspond to the time kL/c required for the low-energy ($\epsilon < \epsilon_b$) light curves to reach steady state, while the dot-dashed and dot-dot-dashed vertical lines correspond to the analytical estimate for the time it takes for the high-energy ($\epsilon > \epsilon_b$) light curves to reach steady state. The pipe orientation is $\theta = \pi/2$ for the top and middle panels and $\theta = 0$ for the bottom panel. The middle panel uses a δ -function approximation for the synchrotron emissivity.

An analytical result regarding the relation of the synchrotron to the SSC emission that we can test our model against addresses the relative amplitude of synchrotron and SSC emission. For states that are synchrotron dominated, an increase of the electron injection normalization results in a linear increase of the synchrotron emissivity, because the synchrotron emissivity is proportional to the number of available electrons, and to a quadratic increase of the SSC luminosity, because the SSC luminosity is proportional to the product of the number of electrons times the

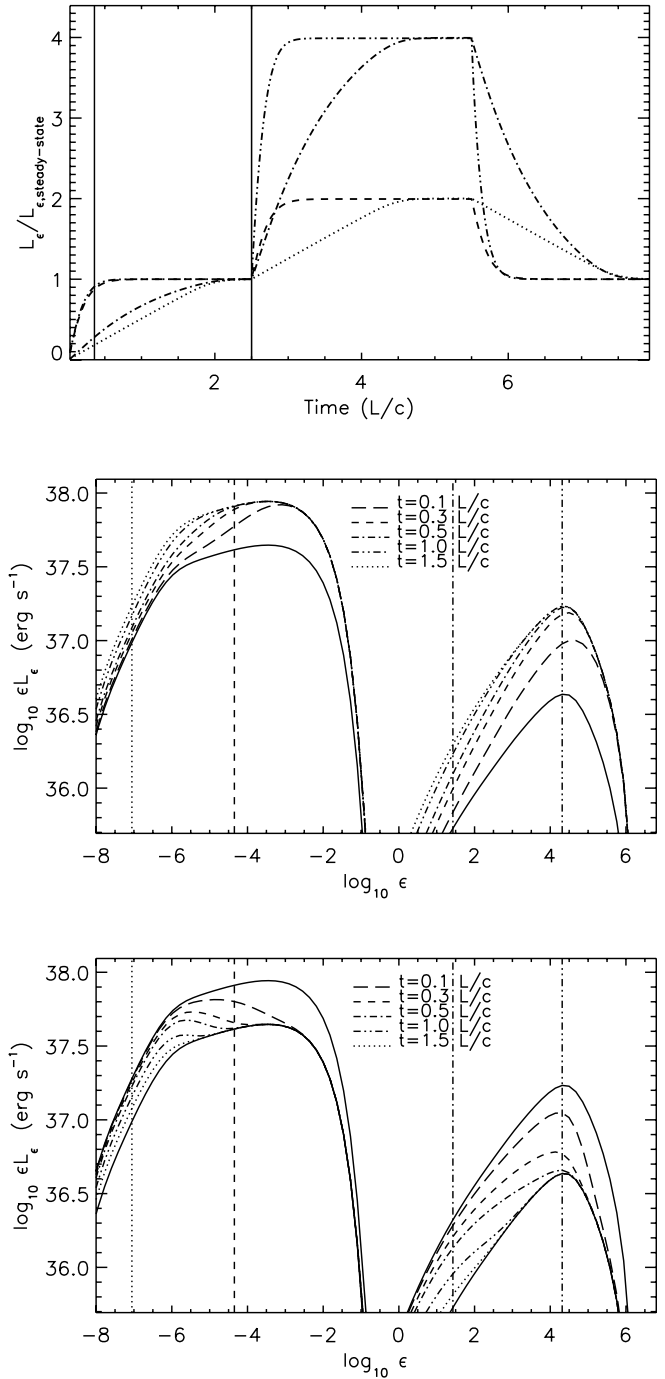


FIG. 4.—Quadratic variation: a doubling of the injected electron power for $t = 3L/c$, a time longer than $2L/c$, the time it takes electrons to traverse the pipe. The initial configuration is the same as that of Fig. 2. *Middle*: Snapshots of the SED for a range of times elapsed from the beginning of the additional injection. *Bottom*: Snapshots of the SED evolution after the additional injection has been switched off. *Top*: Light curves for the four energies depicted by the vertical lines in the bottom two panels.

synchrotron photon energy density, which scales with the number of electrons (e.g., Ghisellini et al. 1996). This result holds as long as the increased injection lasts long enough to occupy the entire volume of the source (in our case $t_{\text{var}} > kL/c$), bringing the source to a new steady state.

To verify that our code reproduces this behavior we start from the configuration of Figure 2, which we observe from an angle $\theta = \pi/2$, and after we let the system reach its steady state, we increase the injected electron luminosity by a factor of 2 for

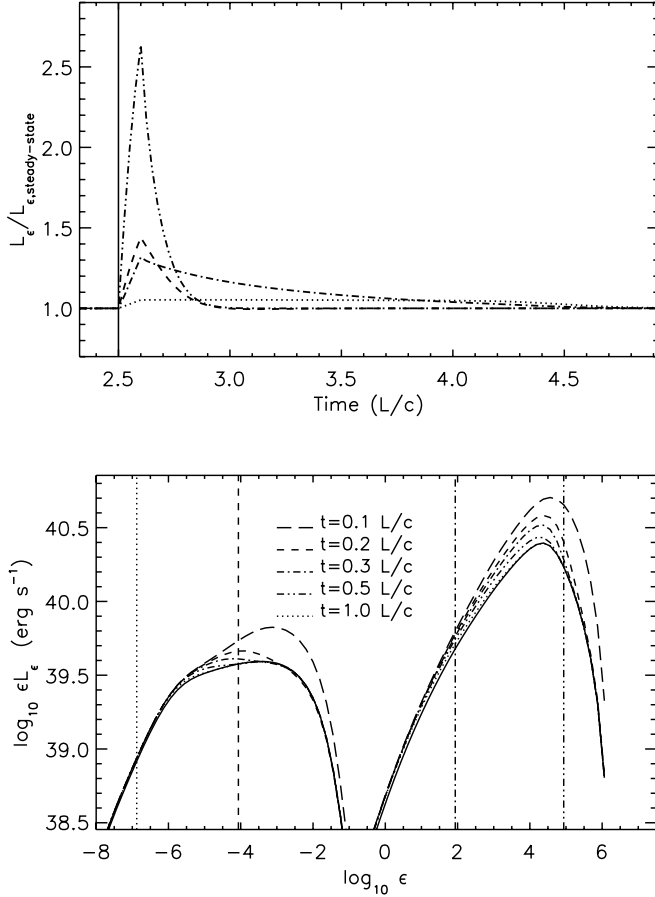


FIG. 5.— Here, we use the same steady state configuration as in Fig. 2, except for higher injected EED luminosity, $L_{\text{inj}} = 5 \times 10^{40}$ ergs s^{-1} . After the system reaches the steady state, we increase the injected luminosity by a factor of 2 for $0.1L/c$. *Bottom*: Evolution of the SED. *Top*: Light curves of the flare for the four energies marked by the vertical lines in the bottom panel.

$t = 3L/c$, longer than $2L/c$, the time to reach steady state. The middle panel of Figure 4 shows the evolution of the SED as the flare grows, with the times denoting the time since the increased injection started, while the bottom panel shows the evolution of the flare as the flare dies out, starting from the time the additional injection is switched off. The characteristic quicker response of the high-energy electrons is apparent. The two solid lines represent the low and high steady states. In the top panel we plot the light curves of the four frequencies marked with vertical lines in the two bottom panels. They are selected to roughly correspond to optical, X-ray, GeV, and TeV energies, assuming that beaming will increase their observed values by a Doppler factor $\delta \sim 20\text{--}40$. Note that the synchrotron emission doubles when it reaches its steady state, while the SSC quadruples, in agreement with the analytical result.

4.2. Case Studies

We present here three variability case studies, for which we use as a starting point the configuration described in Figure 2, increasing the electron luminosity to $L_{\text{inj}} = 5 \times 10^{40}$ ergs s^{-1} to produce a steady state SED (solid line in the bottom panel of Fig. 5) that for a beaming $\delta \sim 20\text{--}40$ resembles those produced by flaring TeV blazars. We first study the case of an increased electron injection that lasts a short fraction of the light crossing time. After the system reaches its steady state, we increase the injected electron luminosity L_{inj} by a factor of 2 for $0.1L/c$. In

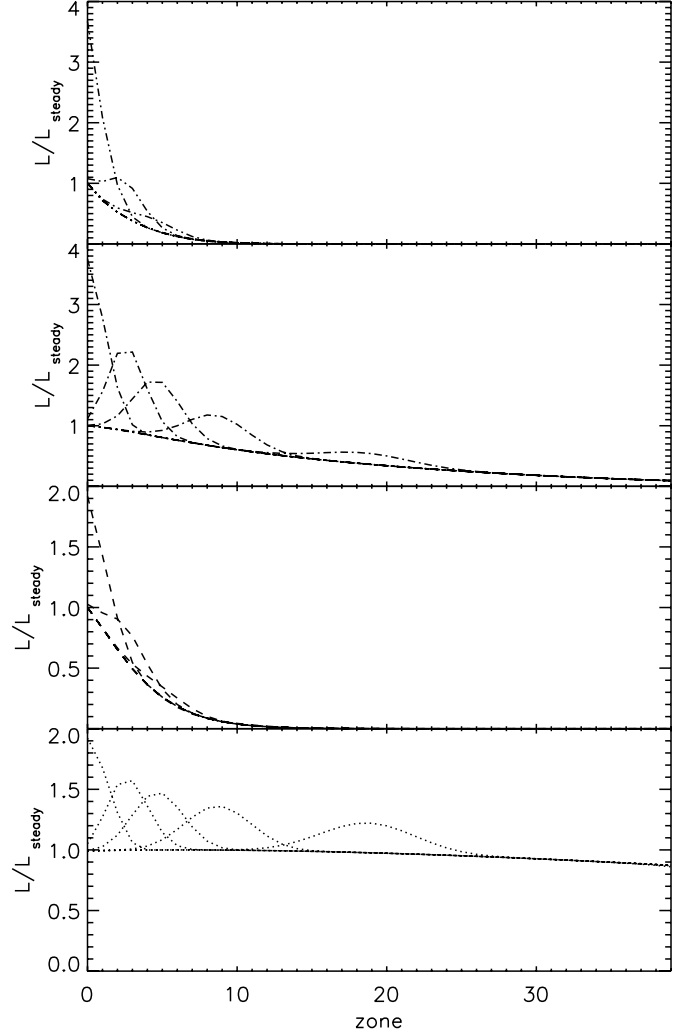


FIG. 6.— Luminosity profile along the pipe for the four energies whose light curves are plotted in Fig. 5, for the same pipe configuration. In each case the bottom line represents the luminosity profile, normalized to the steady state luminosity of the first zone. The profiles at $t = 0.1, 0.2, 0.3, 0.5,$ and 1.0 light crossing times are also plotted and can be seen moving away from the inlet as the additional injection propagates.

the bottom panel of Figure 5, we plot the SED evolution, while in the top panel we plot the light curves that correspond to the four energies denoted by vertical lines in the bottom panel. We note that the flare peaks with no time delays at all energies and then decays with the higher energies of each component decaying first. We also note that both the synchrotron and SSC flare have a higher amplitude at higher energies (and therefore, the spectrum hardens as the flux increases). Also, because additional electrons are injected at all energies, the entire SED responds to the increased injection. The maximum fractional increase of the emission increases with frequency for both the synchrotron and the SSC components. This is because the higher the energy of the electrons required to produce a given synchrotron or SSC emission, the shorter their lifetime in the source; an additional injection, therefore, for a fixed time ($0.1L/c$ in our case) will increase by a higher factor the number of higher energy electrons.

To show how the variability event would be seen if we had the ability to resolve the pipe, we plot in the four panels of Figure 6 the luminosity profile along the pipe for the four energies we study. In all cases we normalize the luminosity to the steady state luminosity of the first zone. The bottom line in all cases depicts the steady state luminosity profile. As expected,

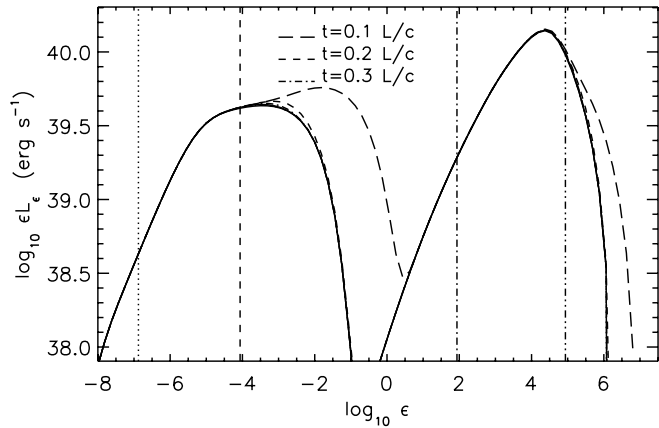
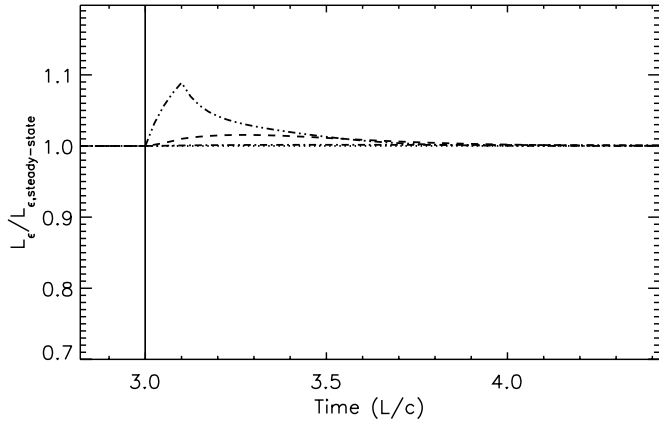


FIG. 7.— Starting from the same steady state as in Fig. 2, γ_{\max} is increased by a factor of 5 for $0.1L/c$.

the high-energy synchrotron and SSC emission is confined close to the inlet, while the low-energy emission of both components extends throughout the source. The decline of the steady state low-energy SSC emission along the pipe is due to the fact that this emission is a convolution of a range of electron energies, and the higher energy electrons are gradually becoming unavailable away from the inlet. On top of the steady states, we plot the snapshot luminosity profiles at the times depicted in the bottom panel of Figure 5. It can be seen how the pulse is propagating away from the inlet, gradually disappearing due to cooling at the high synchrotron and SSC energies. At the low synchrotron and SSC energies it can clearly be seen how the pulse is spreading out due to the escape from zone to zone [the $n(\gamma, t)/t_{\text{esc}}$ term of the kinetic equation]. Note also that while the amplitude of the low-energy synchrotron variation is substantial (starting with an increase by a factor of 2 at the inlet), because the pulse lasts for only $0.1L/c$, and while low-energy synchrotron emission is produced by electrons accumulating for $2L/c$, the increase of the total low-energy synchrotron emission is small (about 5%) as expected and as can be seen in the top panel of Figure 5.

Another possible variation in the injected electron distribution is an increase in the maximum electron Lorentz factor of the EED, something that can result from a temporary increase in the electron acceleration rate. In this case the normalization of the EED remains constant, and the increase in the injected luminosity depends on the electron index and the new value of γ_{\max} . Using the same configuration as above, we increase the value of γ_{\max} by a factor of 5 for the same short time $0.1L/c$ (for an electron index of $p = 1.8$ and for $\gamma_{\min} = 10^3$, this corresponds to an increase of

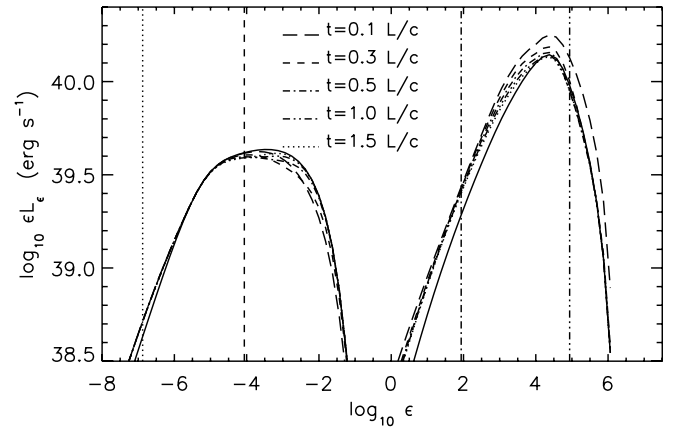
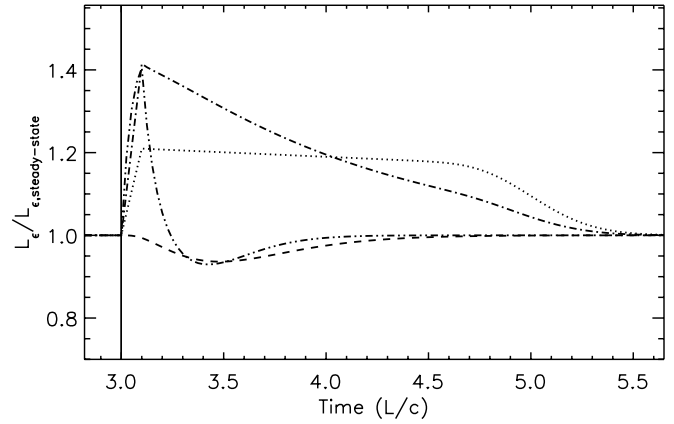


FIG. 8.— Starting from the same steady state as in Fig. 2, we inject for $0.1L/c$ an additional low-energy EED with the same luminosity as the steady injection, but with $\gamma_{\max} = 10^4$.

L_{inj} by $\sim 50\%$), and we follow the evolution of the SED. As can be seen in Figure 7, the event is mostly manifested at the high-energy tails of both the synchrotron and SSC components and dies quickly, because the high-energy electrons injected have very short lifetimes. No significant variations are seen away from the high-energy tails of the synchrotron and SSC components, a notable difference from the previous case in which the normalization of all electrons was increased.

Finally, we study a case in which after the steady state is reached, an additional population of relatively low energy electrons is injected for a short time. This may be a plausible situation if one considers that a preacceleration mechanism is required to accelerate electrons up to Lorentz factors $\gamma \sim \Gamma m_p/m_e$, where Γ is the typical bulk Lorentz factor of the flow, to provide the electrons that can be picked up by the Fermi acceleration mechanism for acceleration to much higher Lorentz factors (e.g., Sikora et al. 2002). Variations in this preacceleration mechanism that are not propagated to Fermi acceleration may account for the variations in the low-energy tail of the electron distribution. We simulate this scenario by injecting an additional low-energy EED with the same luminosity as the steady injection, but with $\gamma_{\max} = 10^4$.

As can be seen in Figure 8, as soon as the injection starts, the additionally injected low-energy electrons produce low-energy synchrotron emission (dotted line in Fig. 8) that remains at a plateau during the time it takes for the extra injection to traverse the length of the pipe, because these low-energy electrons do not cool strongly. In the beginning, these low-energy synchrotron photons are produced close to the TeV energy electrons of

the steady flow (due to radiative losses these high-energy electrons are found only close to the injection inlet) and are up-scattered by them to TeV energies, producing additional TeV emission which is manifested as the rising part of the TeV flare (dot-dot-dashed line). As the event evolves, the additional population of low-energy electrons propagates downstream, and due to the increasing distance between the additionally produced synchrotron photons and the pipe inlet where the TeV electrons are found, the TeV flare quickly subsides. The behavior of the X-ray emission (dashed line) is very interesting; the extra low-energy synchrotron photons produced increase the photon density experienced by the synchrotron X-ray-emitting electrons, and this causes additional cooling, slightly reducing the X-ray synchrotron emission. As the production of these additional low-energy synchrotron photons is displaced downstream, their effect at the neighborhood of the inlet, where the synchrotron-emitting electrons are found, decreases, and the X-ray flux returns to its steady state. The behavior of the lower energy γ -ray emission does not show the sharp decline of the high-energy γ -rays. Instead, their light curve shows a gradual decline. This flare is mostly produced by the additional electrons upscattering a broad energy range of seed photons that have a gradually decreasing energy density with distance from the inlet energy. The model behavior of a TeV flare not accompanied by an X-ray flare is reminiscent of the so-called orphan TeV flares (Krawczynski et al. 2004; Błażejowski et al. 2005). These are rare flaring states of blazars characterized by an increase in the TeV luminosity that is not accompanied by a similar increase in X-ray energies.

5. DISCUSSION AND FUTURE WORK

We presented a multizone code that for the first time takes into account the nonlocal, time-retarded nature of SSC losses. This code is currently the only multizone model that incorporates the nonlocal, time-delayed SSC losses and, as such, is uniquely suitable for modeling the results of multiwavelength campaigns at radio, optical, X-ray, and γ -ray energies, and particularly the observations of ground-based TeV and *Fermi* GeV variability of blazars.

As we argued, the results of one-zone codes for the critical high-energy regime of both the synchrotron and SSC components are problematic and should not be used to infer the physical conditions in the source through variability modeling. We described our multizone code, tested it successfully against known analytical results, and presented a small number of variability case studies. The case studies we presented, although based on the same underlying steady state configuration, exhibited very different variability patterns. This means that detailed modeling of broadband SEDs and simultaneous multiwavelength variability can be used to infer what is actually the cause of a given observed variability pattern, providing reliable constraints on the particle acceleration taking place. Orphan flares can be reproduced assuming an increase of the injection of the low-energy electrons, but not assuming the injection of a very high energy electron population, as we also showed analytically. The fact that this plausible variation cannot produce orphan flares significantly narrows the parameter space for events that can produce such events, possibly in agreement with their observed scarcity.

The code we described can run on a typical workstation in a reasonable time of at most a few minutes at a resolution of ~ 10 bins per decade of observing frequency, ~ 10 bins per decade of electron energy, and ~ 50 zones. To achieve this we employed a pipe geometry and adopted an energy-conserving δ -function approximation for the SSC emissivity, as well as a step function approach to take into account the change from the Thomson to Klein-Nishina IC-scattering cross sections. Adopting these ap-

proximations is problematic for situations where IC scattering of narrow photon distributions (e.g., line emission from the broad-line region or even a blackbody spectrum characterized by a typical photon energy ϵ_0) is important. In this case, the adoption of the step function cross section description would create a strong artificial feature on the EED localized at the transition from the Thomson to the Klein-Nishina regimes at $\gamma \propto 1/\epsilon_0$, which would then propagate to the emitted spectra through the δ -function IC emissivity. For SSC systems, however, where the seed photons are spread over many decades in energy, the resulting spectra are good approximations of those produced using the full expressions for the synchrotron and SSC emissivities as well as the full Klein-Nishina cross section.

Including the above considerations, as well as the processes of synchrotron opacity and pair production through γ -ray absorption within the source, would increase the execution time up to levels marginally comfortable for the typical workstation. Most probably, such an extension of the code would require parallelization. A more desirable upgrade of the code would drop the assumption of no lateral gradients in the plasma characteristics by switching to a two-dimensional geometry, in which the electron distribution and the SSC photon energy density are allowed to change laterally to the flow direction. Such considerations may be relevant to the recently observed ~ 0.75 days delay between the IR and the X-ray variability in 3C 273 (McHardy et al. 2007). These authors argued that the delay may be attributed to the time it takes for the SSC photon energy density to build up as the SSC photons are traversing the cross section of the flow. This upgrade will scale the computation time roughly by N^2 , increasing it from \sim few minutes to \sim several hours. We note here that our formalism can be extended to treat velocity profiles in terms of the decelerating flow (Georganopoulos & Kazanas 2003) or the spine sheath model (Ghisellini et al. 2005) that have been developed to address the lack of superluminal motions in TeV blazars (e.g., Piner & Edwards 2004).

Another upgrade that can be incorporated in the existing code, this time with a minimal computational overhead, is that of a zone for particle acceleration, following the formalism of Kirk et al. (1998). In this case, in the first zone of the model, low-energy electrons will be injected and allowed to accelerate while suffering radiative losses due to synchrotron and nonlocal SSC. These particles will subsequently escape into the pipe and flow downstream. This configuration will require a different numerical scheme for the acceleration zone, since there, most particles are advected upward in energy space, but there is a possibility, in a time-dependent scenario, of the highest energy particles being advected downward, while the rest of the electrons are still advected upward. The benefit of including particle acceleration in the code is that it will allow us to study cases of hard lags/ counterclockwise loops in the X-ray hardness–X-ray flux diagrams thought to result when acceleration and loss timescales are comparable. Such a code could be used to model the observed curved X-ray spectra of high peak frequency blazars in the framework of episodic particle acceleration (Perlman et al. 2005).

We are grateful to the referee for a critical review of the first version of the manuscript that made us aware of some important limitations of the first version of our code. Part of this work was done in the context of the senior thesis of Philip Graff at UMBC. The authors acknowledge support from NASA LTSA grants NAG 05-9997 and NNG 05-GD63G at UMBC, from NNX 07-AM17G at FIT, and from the Chandra theory grant TM6-7009A at UMBC.

REFERENCES

- Aharonian, F. A. 2000, *NewA*, 5, 377
- Aharonian, F. A., et al. 2005, *A&A*, 442, 895
- . 2007, *ApJ*, 664, L71
- Begelman, M. C., Fabian, A. C., & Rees, M. J. 2008, *MNRAS*, 384, L19
- Blandford, R. D. 1978, in *Pittsburgh Conf. on BL Lac Objects*, ed. A. N. Wolfe (Pittsburgh: Univ. Pittsburgh Press), 328
- Błażejowski, M., Sikora, M., Moderski, R., & Madejski, G. M. 2000, *ApJ*, 545, 107
- Błażejowski, M., et al. 2005, *ApJ*, 630, 130
- Böttcher, M. 2007, *Ap&SS*, 309, 95
- Chang, J. S., & Cooper, G. 1970, *J. Comput. Phys.*, 6, 1
- Chiaberge, M., & Ghisellini, G. 1999, *MNRAS*, 306, 551
- D'Arcangelo, F. D., et al. 2007, *ApJ*, 659, L107
- Fossati, G., et al. 2000, *ApJ*, 541, 153
- . 2008, *ApJ*, 677, 906
- Georganopoulos, M., & Kazanas, D. 2003, *ApJ*, 594, L27
- Georganopoulos, M., & Marscher, A. P. 1998a, *ApJ*, 506, 621
- . 1998b, *ApJ*, 506, L11
- Ghisellini, G., Maraschi, L., & Dondi, L. 1996, *A&AS*, 120, C503
- Ghisellini, G., Tavecchio, F., & Chiaberge, M. 2005, *A&A*, 432, 401
- Gómez, J. L., Alberdi, A., Marcaide, J. M., Marscher, A. P., & Travis, J. P. 1994, *A&A*, 292, 33
- Graff, P. B., Georganopoulos, M., Perlmutter, E. S., & Kazanas, D. 2007, in *AIP Conf. Proc. 921, The First GLAST Symposium*, ed. S. Ritz, P. Michelson, & C. A. Meegan (Melville: AIP), 333
- Harding, A. K., & Lai, D. 2006, *Rep. Prog. Phys.*, 69, 2631
- Kardashev, N. S. 1962, *Soviet Astron.*, 6, 317
- Kataoka, J., Takahashi, T., Makino, F., Inoue, S., Madejski, G. M., Tashiro, M., Urry, C. M., & Kubo, H. 2000, *ApJ*, 528, 243
- Katarzyński, K., Ghisellini, G., Tavecchio, F., Gracia, J., & Maraschi, L. 2006, *MNRAS*, 368, L52
- Kirk, J. G., Rieger, F. M., & Mastichiadis, A. 1998, *A&A*, 333, 452
- Krawczynski, H., Coppi, P. S., & Aharonian, F. 2002, *MNRAS*, 336, 721
- Krawczynski, H., et al. 2004, *ApJ*, 601, 151
- Maraschi, L., Ghisellini, G., & Celotti, A. 1992, *ApJ*, 397, L5
- Maraschi, L., et al. 1999, *ApJ*, 526, L81
- Marscher, A. P., et al. 2008, *Nature*, 452, 966
- Mastichiadis, A., & Kirk, J. G. 1997, *A&A*, 320, 19
- McHardy, I., Lawson, A., Newsam, A., Marscher, A. P., Sokolov, A. S., Urry, C. M., & Wehrle, A. E. 2007, *MNRAS*, 375, 1521
- Melrose, D. 1980, *Plasma Astrophysics*, Vol. 1 (New York: Gordon & Breach)
- Perlmutter, E. S., et al. 2005, *ApJ*, 625, 727
- Piner, B. G., & Edwards, P. G. 2004, *ApJ*, 600, 115
- Piner, B. G., Pant, N., & Edwards, P. G. 2008, *ApJ*, 678, 64
- Ravasio, M., Tagliaferri, G., Ghisellini, G., & Tavecchio, F. 2004, *A&A*, 424, 841
- Sambruna, R. M., et al. 2000, *ApJ*, 538, 127
- Sikora, M., Begelman, M. C., & Rees, M. J. 1994, *ApJ*, 421, 153
- Sikora, M., Błażejowski, M., Moderski, R., & Madejski, G. M. 2002, *ApJ*, 577, 78
- Sokolov, A., & Marscher, A. P. 2005, *ApJ*, 629, 52
- Sokolov, A., Marscher, A. P., & McHardy, I. M. 2004, *ApJ*, 613, 725
- Takahashi, T., et al. 1996, *ApJ*, 470, L89
- Zhang, Y. H. 2002, *MNRAS*, 337, 609